AIAA JOURNAL
Vol. 49, No. 5, May 2011

Influence of Random Residual Stress on Fretting Fatigue

Michael P. Enright,* Kwai S. Chan,† and Jonathan P. Moody‡
Southwest Research Institute, San Antonio, Texas 78238
Patrick J. Golden§
U.S. Air Force Research Laboratory, Wright–Patterson Air Force Base, Ohio 4543
and
Ramesh Chandra¶ and Alan C. Pentz**
NAVAIR, Patuxent River, Maryland 20670

DOI: 10.2514/1.45774

Probabilistic risk assessment has increasingly been adopted by certification agencies to address the inherent uncertainties in fatigue crack nucleation and growth processes. Fretting fatigue is a significant damage source for aircraft gas turbine engine components. When present, it can reduce component lives by 40 to 60 percent or more. Surface treatments introduce compressive residual stresses that have the potential to substantially increase component lifetimes. In this paper, an approach is presented for estimating the fretting fatigue risk reduction associated with surface treatment of an actual military engine disk under real-life loading conditions. Residual stresses associated with surface treatment are based on values reported in the literature. A probabilistic model of the fretting process is calibrated based on available failure data and used to quantify the influence of surface treatment on the probability of fracture.

Nomenclature

a	=	crack depth
C	=	empirical constant for the power-law region of the NASGRO equation
c	=	half surface crack length
d	=	decay distance in the residual stress profile
E	=	Young's modulus
F_{blade}	=	radial force of the blade acting on the disk slot
f	=	ratio of $K_{\text{op}}/K_{\text{max}}$
$g(\boldsymbol{X}, \boldsymbol{Y}, N)$	=	failure limit state
K	=	stress intensity factor
$K(\boldsymbol{X}, \boldsymbol{Y}, N)$	=	stress intensity factor
K_c	=	fracture toughness
K_{max}	=	maximum stress intensity factor value
K_{op}	=	stress intensity factor at which the crack tip is fully open
M	=	contact moment per unit thickness
N	=	number of flight cycles
n	=	empirical constant for the power-law region of the NASGRO equation
P	=	normal contact force per unit thickness
p	=	empirical constant describing the large-crack threshold region of the NASGRO equation
$p(x)$	=	contact pressure traction
Q	=	shear contact force per unit thickness
q	=	fast fracture region of the NASGRO equation
$q(x)$	=	contact shear traction
S	=	bulk stress
t	=	thickness of disk slice
$\boldsymbol{X}$	=	vector of input variables unrelated to inspections
x_0	=	center of contact
$\boldsymbol{Y}$	=	vector of input variables related to inspections
α	=	slope of shear force versus normal force in partial slip
$\Gamma(\,)$	=	gamma function
ΔK_{th}	=	large-crack growth threshold
θ	=	flank angle of the dovetail
μ	=	coefficient of friction
ν	=	Poisson's ratio
σ_c	=	compressive stress component in the residual stress profile
σ_{ij}	=	components of stress
σ_t	=	and tensile stress component in the residual stress profile
σ_{xx}	=	crack opening stress
Ω	=	fan rotor speed

Presented as Paper 2009-2302 at the 11th AIAA Non-Deterministic Approaches Conference, Palm Springs, CA, 4–7 May 2009; received 1 June 2009; revision received 19 May 2010; accepted for publication 25 October 2010.

*Principal Engineer, Reliability and Materials Integrity, 6220 Culebra Road. Member AIAA.
†Institute Scientist, Materials Engineering, 6220 Culebra Road.
‡Research Engineer, Reliability and Materials Integrity, 6220 Culebra Road. Member AIAA.
§Materials Research Engineer, Metals, Ceramics and NDE Division, 2230 Tenth Street, Suite 1. Senior Member AIAA.
¶Life Management Engineer, Propulsion and Power Engineering, Structural Integrity Branch, 22195 Elmer Road, Building 106.
**Manager, Propulsion and Power Engineering, Structural Integrity Branch, 22195 Elmer Road, Building 106.

I. Introduction

FATIGUE crack nucleation and growth of metals is dependent on a number of variables that are inherently random in nature. Probabilistic risk assessment has therefore been increasingly adopted by government certification agencies to supplement the traditional safe-life approach that is commonly used for assessment of high-energy rotating components in aircraft gas turbine engines. For example, the U.S. Federal Aviation Administration has released several advisory documents [1,2] over the past several years that recommend the use of probabilistic methods for risk assessment of aircraft engine components. The fatigue crack growth process is commonly modeled using random variables related to the size and location of the initial crack, variability associated with applied stress and crack growth life models, and uncertainty in the quality and frequency of nondeterministic inspections [3]. Probabilistic models are well established for the nucleation or initiation phase and typically focus on adjustment of stress-life models [4–6] and

assignment of random variables to the regression coefficients associated with failure data [7,8].

Fatigue cracks can also be initiated by fretting, a process that occurs when two components are placed in contact and subjected to cyclic loads of relatively small (i.e., less than about 100 μm) displacement [9,10]. Fretting fatigue has been identified as one of the costliest sources of in-service damage related to high-cycle fatigue in the U.S. Air Force [11]. Component lifetimes can be reduced by as much as 40–60% or more depending on the severity of the loading [4,12]. The stresses associated with fretting also influence the crack growth phase, severely reducing component lifetimes [9,13–16]. In fact, a review of experimental observations suggests that fretting fatigue is dominated by the fatigue crack growth phase [17], in which the crack initiation life is often shorter than the crack propagation life. Stress values in the contact region often have the most influence on small cracks for which traditional long-crack fracture mechanics may not apply. Small-crack fretting models have recently emerged to address this issue [18–20].

Surface treatments introduce compressive residual stresses that have the potential to substantially improve the lifetimes of components subjected to fatigue [21–23]. For example, the compressive residual stresses induced by shot peening (SP) have been shown to increase fatigue life by delaying crack initiation or crack propagation [21,22,24,25]. Unfortunately, the surface roughness and damage introduced by SP can promote fatigue crack initiation at shot-peened surfaces, leading to lower fatigue life under certain conditions [26,27]. In recent studies, advanced techniques such as laser shock peening (LSP) and low-plasticity burnishing (LPB) have been shown [21,23] to produce deep-penetrating compressive stresses without producing undesirable surface damage [24,25]. As in SP, the compressive residual stresses introduced by LPB or LSP may relax to lower magnitudes after thermal exposure to higher temperatures or fatigue cycling [21,23]. Thus, there is a need to assess the effectiveness of compressive residual stresses in mitigating fretting fatigue in an engine environment.

In this paper, an approach is presented for estimating the risk reduction associated with surface treatment of aircraft engine components subjected to fretting fatigue. The approach is illustrated for an actual military engine disk under real life loading conditions. Stresses in the blade–disk contact region are estimated using a fine mesh finite element model coupled with a singular integral equation (SIE) solver. Residual stresses associated with surface treatment are based on values reported in the literature [21]. These values are superimposed on the bulk stress values and applied to the computation of the local stress intensity factor range, the local stress ratio, and the corresponding crack propagation rate for a mode I fretting fatigue crack. A probabilistic model of the fretting process is formulated and calibrated using available failure data from an existing engine fleet. The resulting calibrated model is used to quantify the influence of surface treatment on the probability of fracture of military engine disks subjected to fretting fatigue.

II. Contact Stress Modeling

The loads and associated stresses in the blade–disk region of an engine disk can be estimated using nonlinear contact analysis. Calcaterra and Naboulsi [28] investigated contact damage in blade and disk attachments from the compressor stage of two similar military engines. They concluded that a finite element method (FEM) analysis was not sufficient to predict the stresses at the edge of contact. Instead, they implemented a hybrid process in which both FEM and the SIE solution tool CAPRI were applied. Golden and Calcaterra [29] showed that fracture mechanics methods using the contact stress analysis can be used to predict the lives of dovetail fretting fatigue specimens. That analysis, however, was not applied to real components, and was confined to constant amplitude loading. Gean and Farris [30] demonstrated a method to predict contact forces for a prescribed engine speed and thermal mission. This type of methodology is necessary for practical assessment complex missions when using FEM component contact analyses.

The normal contact force per unit thickness P associated with fretting can be obtained by integration of the pressure $p(x)$ in the contact region over the contact length x:

$$P = \int p(x)\,\mathrm{d}x \tag{1}$$

Prior work has shown that contact forces can be accurately predicted even with fairly coarse meshes [28]. Likewise, the shear traction, $q(x)$, can be integrated over the contact length to obtain the shear contact force per unit thickness, Q:

$$Q = \int q(x)\,\mathrm{d}x \tag{2}$$

The contact moment per unit thickness M about the center of contact is equal to the integral of the product of the contact pressure p and the distance from the center of contact, x_0:

$$M = \int (x - x_0)\,p(x)\,\mathrm{d}x \tag{3}$$

The vector relationship among the contact forces P, Q and moment M is described in [30]. The scalar relationship among contact forces P and Q is illustrated in Fig. 1 for a typical fan speed profile. In Fig. 1, the dashed lines indicate the bounds imposed by the coefficient of friction μ. When $Q = \mu P$, the contact is called "sliding" or "gross slip." When $|Q| < \mu P$ the contact is referred to as "partial slip." The slope α of the Q versus P curve during partial slip is a characteristic of the component. This slope is used to predict more complex histories of Q and P as described later in the paper.

Contact stresses can be obtained directly from the contact forces and moments using the numerical solution of the SIE that characterizes the contact interface using the CAPRI software [31] or the worst case fret (WCF) model [32]. The CAPRI SIE solver was developed to calculate contact stresses for a random shaped indenter pressing into a flat plate with a shear force applied using a Fourier transform technique [31].

The WCF model [32] was developed to treat the propagation and arrest of small cracks under the influence of the fretting stress field in the presence of a remotely applied bulk stress. The WCF model considers a flat pad subjected to a normal load P, a shear force Q, and bulk stress S (see [32] for more details regarding the model). The contact stress field for the flat pad can be obtained for a given set of P and Q values.

The distributions of normal traction, $p(x)$, and shear traction, $q(x)$, on the fretting surfaces are first computed using the singular-integral-equations formulation by Ciavarella et al. [33]. Series expansions are then performed for $p(x)$ and $q(x)$ in terms of Chebyshev's polynomials, which are then used to obtain the Mushkelishivili potential. Subsequently, the interior stress field (i.e., the stress in the interior of the component associated with contact forces) is evaluated from Mushkelishivili's potential using standard equations to obtain the fretting fatigue stresses. The results are added to the bulk stress to obtain the total stresses. The total stresses are then used to compute

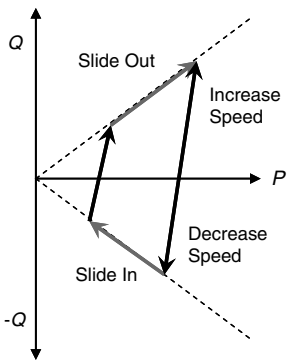

Fig. 1 Illustration of the relationship among contact forces P and Q in the disk–blade interface of a typical gas turbine engine.

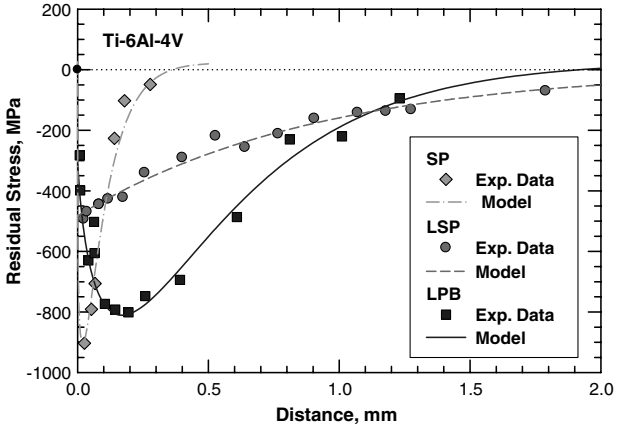

Fig. 2 Comparisons of residual profiles produced by SP, LSP, and LPB and model calculations fitted to experimental data [21].

the stress intensity factors and fatigue crack growth rate response. Details of the governing equations and the computational procedures were reported in an earlier paper [32].

III. Residual Stress Model

The residual stress profile in the attachment region of an engine disk depends heavily on the processing method and parameters. At least three processing methods including SP, LSP, and LPB have been considered for imparting residual stresses in engine disks [21]. A comparison of the residual stress profiles produced by SP, LSP, and LPB [21] is shown in Fig. 2, which shows that differences exist in the level and the extent of the compressive stresses in the residual stress zone.

The residual stress profile is typically described using empirical expressions fitted to experimental data obtained by x-ray diffraction methods [22,34]. The functional form of the residual stress expression generally contains an exponential decay term for the compressive residual stress [22,34]. Incorporating the tensile residual term may require a uniform stress or a sinusoidal term [34]. For simplicity, an exponential decay function is used to describe both the compressive stress (σ_c) and tensile stress (σ_t) components in the residual stress profile. This expression is given by

$$\sigma_{\mathrm{RS}} = -\sigma_c\left(\frac{x}{b}\right)^c \exp\left(-\frac{x-a}{b}\right) + \sigma_t \exp\left(-\frac{x}{d}\right) \tag{4}$$

in which σ_c, σ_t, a, b, c, d are empirical constants evaluated from experimental data of residual stresses. To determine the constants, the values of σ_c, a, b, and c are evaluated for a given compressive stress profile. Subsequently, the tensile stress profile is determined as one that balances the compressive stress values so that the net residual stress is zero. On this basis,

$$\sigma_t = \sigma_c\left(\frac{b}{d}\right)\exp\left(\frac{a}{b}\right)\Gamma(1+c) \tag{5}$$

in which $\Gamma(1+c)$ indicates the value of the gamma function with an argument of $1+c$. The decay distance d is evaluated by fitting Eq. (5) to match the experimental tensile stress distribution. The residual stress profiles associated with these constants are compared against the experimental data in Fig. 2. Goodness of fit values (i.e., R^2) for the least-square fits are 0.9358 or better with a standard error that is 0.0823 or less, as shown in Table 1.

IV. Probabilistic Crack Growth Life

Given an initial anomaly in a rotor disk subjected to variable amplitude loading, the stress intensity factor K increases with increasing number of flight cycles. Failure occurs when the maximum K exceeds the fracture toughness K_c:

$$g(\boldsymbol{X}, \boldsymbol{Y}, N) = K_C - K(\boldsymbol{X}, \boldsymbol{Y}, N) \le 0 \tag{6}$$

$g(\boldsymbol{X}, \boldsymbol{Y}, N)$ is dependent on two general input variable vectors ($\boldsymbol{X}$, a vector of input variables unrelated to inspections, and $\boldsymbol{Y}$, a vector of input variables related to inspections):

$$g(\boldsymbol{X}, \boldsymbol{Y}, N) = g(X_1, \ldots, X_n; Y_1, \ldots Y_m; N) \tag{7}$$

A negative or zero $g(\boldsymbol{X}, \boldsymbol{Y}, N)$ represents a failure event. The probability of fracture is

$$P_f = P[g(\boldsymbol{X}, Y, N) \le 0] \tag{8}$$

The crack growth rate values can be obtained using a NASGRO equation [35] fit of the material data. The NASGRO equation describes all three regions of the large-crack FCG curve and is given by

$$\frac{\mathrm{d}a}{\mathrm{d}N} = C\left(\frac{(1-f)\Delta K}{1-R}\right)^n \frac{(1-\frac{\Delta K_{\mathrm{th}}}{\Delta K})^p}{(1-\frac{K_c}{K_{\max}})^q} \tag{9}$$

The parameter p is an empirical constant describing the large-crack threshold region, ΔK_{th}, and the parameter q describes the fast fracture region in which the maximum K, $K_{\max}$, approaches the critical stress intensity at fracture, K_C. The parameter f is the ratio of $K_{\mathrm{op}}/K_{\max}$, in which K_{op} is the stress intensity factor at which the crack tip is fully open. The presence of a compressive residual increases K_{op} and thus reduces the effective ΔK, which is the difference between $K_{\max}$ and K_{op}. The value of f is computed using the Newman crack-closure model [35].

V. Application to Aircraft Engine Disks

The probabilistic methodology was applied to an actual military engine disk under real life loading conditions. A finite element analysis was performed to obtain the contact forces which were converted to stress values and applied to assess the risk of fracture and risk reduction associated with surface treatments.

A. Contact Stresses

A FEM analysis of the disk–blade assembly was carried out to obtain contact forces and moments along the disk–blade interface associated with applied inertial and static aerodynamics forces on the airfoil. Because the complex geometry of the fan blade, quadratic tetrahedral elements were used for the associated finite element mesh. A refined mesh of first-order hexahedral elements was used for the dovetail portion of the fan blade and the disk [36]. This element type was selected for its superior performance in the contact interface.

The final mesh for the disk–blade assembly and for the interface region between the dovetail portion of the blade and the disk is shown in Figs. 3a and 3b. The dovetail is aligned along the axial direction of the engine. A single blade and section of the disk were modeled using cyclic symmetry to represent the entire rotor. The model was solved using the ABAQUS software using a surface-to-surface contact formulation [37] with a coefficient of friction among surfaces analyzed. Figure 3c is a front view of the disk sector in the model with

Table 1 Material constants for LPB, LSP, and SP residual stress profiles

Process	a, mm	b, mm	c	σ_c, MPa	σ_t, MPa	d, mm	$\Gamma(1+c)$	R^2	Standard error
LBP	3.08E − 01	3.87E − 01	4.63E − 01	860	2.61E + 01	25.0E + 00	8.86E − 01	0.9358	0.0823
LSP	0.00E + 00	8.42E − 01	0.00E + 00	520	8.76E + 00	5.00E + 01	1.00E + 00	0.9811	0.047
SP	3.39E − 02	7.88E − 02	7.88E − 02	1100	2.41E + 01	5.00E + 00	9.06E − 01	0.9979	0.025

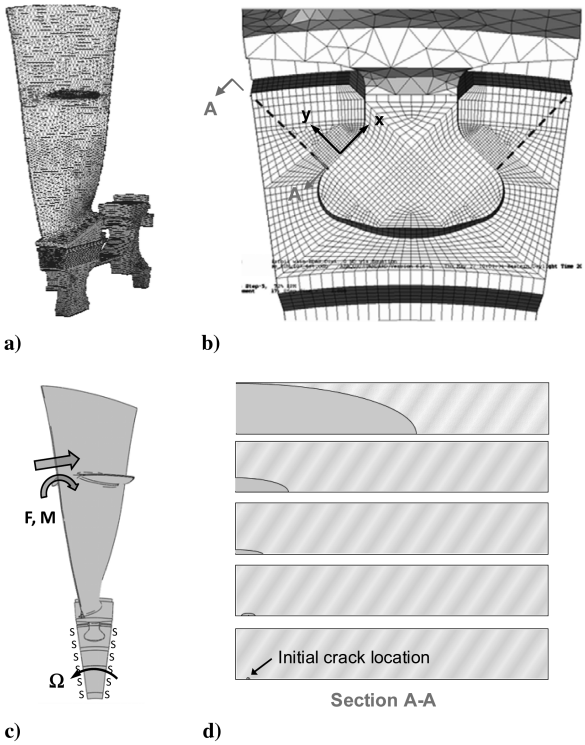

Fig. 3 Finite element model of disk–blade interface subjected to fretting fatigue: a) higher-order tetrahedral elements used to model the complex geometry of the fan blade, b) refined mesh of first-order hexahedral elements used for the dovetail portion of the fan blade and disk, c) diagram showing the external forces and boundary conditions, and d) initial crack location and associated propagation path.

the blade attached showing external forces and boundary conditions. External forces include: 1) the centrifugal force due to rotational speed Ω applied to all elements of the model and 2) the aerodynamic forces applied to the airfoil nodes (represented in Fig. 3 by force F and moment M). The cyclic symmetry of the sector model was enforced by introducing boundary conditions based on the constraint equations at the cut surfaces of the disk sector (represented as sector S boundary conditions in Fig. 3). Note that a single node on the underside of the disk sector was fixed in the axial direction to prevent rigid body motion. The initial crack location and associated propagation path are shown in Fig. 3d.

Contact forces were identified using Eqs. (1–3). Note that the units for the contact forces are force per unit thickness and moment per unit of thickness in which thickness was the material associated with a single slice through the FE model. The Q versus P history for a representative slice is shown in Fig. 4. The FEM analysis results were also used to estimate the bulk stress values, defined as the stress in the component in the absence of the local contact stresses (i.e., the stress

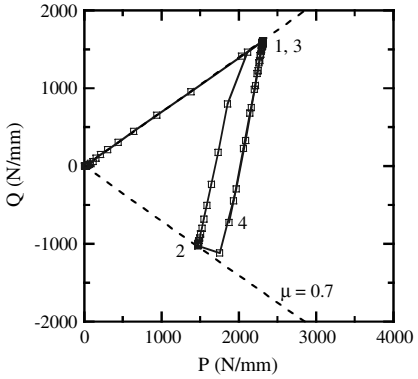

Fig. 4 Contact force history for a representative slice of finite element model: 1) 110% maximum speed, 2) 50%, 3) 110%, and 4) 72%.

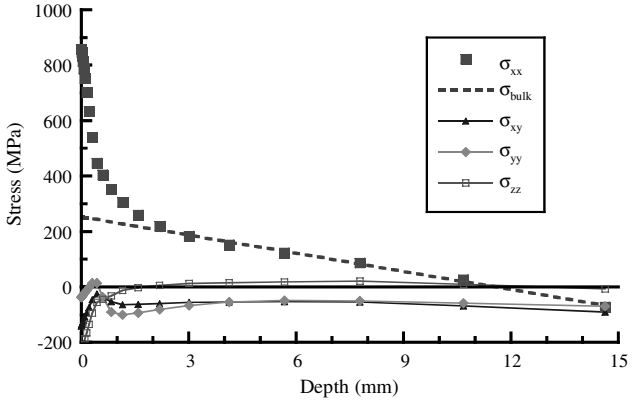

Fig. 5 Bulk stresses were obtained from the finite element model along a path perpendicular to the edge of contact for a single load increment.

due to the inertial load of the disk only). To obtain the bulk stress values, the multi-axial components of stress were extracted from the FEM results along a path perpendicular to the contact interface starting at the edge of contact. This path is shown in Fig. 3b as a dashed line on both the high-pressure and low-pressure side of the dovetail slot.

Stress values were extracted from the FEM results for each load increment. An example is shown in Fig. 5, in which x is parallel to the contact surface in the plane of the slice, y is in the direction of the path, and z is out of the plane in the axial direction of the slot, as shown in Fig. 3b. As expected, the crack opening stress σ_{xx} was clearly the dominant component of stress (although it included some influence from the contact interface). This stress gradient, however, could not simply be used as the contact stress because it was not converged. The contact stress at the edge of contact had a very high and localized elastic peak that could not be captured in a three-dimensional FE model due to the unachievable mesh refinement and computational time requirements to do so. Instead, the FE results were used to capture only the bulk stress portion of the total stress results and, therefore, the near surface portion was ignored and the remainder was linearly fit and extrapolated back to the surface to obtain σ_{bulk}. This approach appears to provide reasonable results. The other multi-axial components of stress were not included in this analysis since they were relatively small.

The simplified mission profile described earlier (0, 110, 50, 110, 72%) was used for the finite element analysis for two reasons: 1) to limit the computational time needed for the analysis and 2) because the aerodynamic loads were only available at those speeds. The actual mission for the component of interest was more complex than the one used in the FE analysis. It was represented using the composite mission shown in Fig. 6, which consists of 32 speed reversals and includes both major and minor reversals.

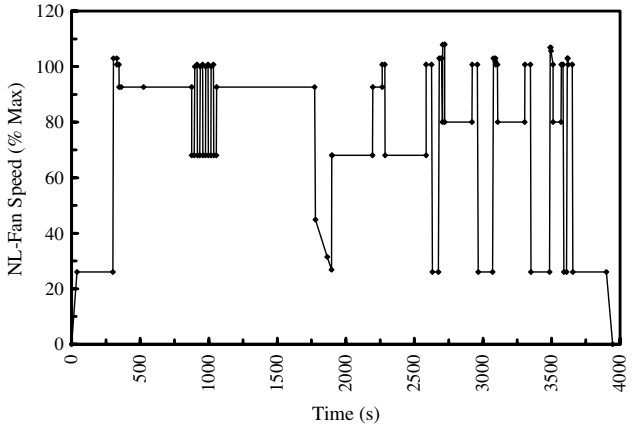

Fig. 6 Typical fan speed profile based on the composite mission associated with actual engine usage histories.

A method was needed to predict the contact forces and bulk stress for this mission given the results of the FEM analysis, such as the method developed by Gean and Farris [30]. In general, the predictions could incorporate changes in both speed and temperature. However, the disk was assumed to be under isothermal conditions, so stress values associated only with speed changes were considered. The moment remained small and constant with speed for all the dovetail slot slices considered. Also, it was found that the bulk stress was nearly proportional to the square of the speed, so the discussion will be limited to P and Q.

Several constraints were applied to predict the P and Q history given the speed history and are included as Eqs. (10–12). P and Q are subscripted with the index i, since the equations applied to individual slices. As indicated in Eq. (10), the sum of the radial components of P and Q times their slice thickness t must equal the total radial force applied by the blade. This blade force is proportional to the square of the rotor speed Ω:

$$F_{\text{blade}} = \sum [t_i \cdot (P_i \cos\theta + Q_i \sin\theta)] \propto \Omega^2 \tag{10}$$

The relationship among blade forces and rotor speed is shown conceptually in Fig. 3c. An example prediction of Q versus P is shown in Fig. 7 for the mission shown in Fig. 6. Initially, the blade "slides out" in the slot due to the frictional shear force exceeding that required for slip and following the dashed line defined by

$$|Q_i| \leq \mu P_i \tag{11}$$

Next, the speed decreases but the blade remains wedged or stuck in place and the Q versus P path follows the slope α down as described by Eq. (12):

$$\Delta Q_i = \alpha_i \Delta P_i \tag{12}$$

If the speed decreases enough, however, the blade will become unstuck and "slide in," which is shown by the lower dashed line in Fig. 7. When speed increases again, P and Q move up along slope α until the upper dashed line is reached then the blade again slides out.

The CAPRI [31] and WCF [32] models were used to compute the contact stresses associated with a blade fretting on a disk. The input parameters to both models included the Young's modulus (E= 107 GPa), Poisson's ratio ($\nu = 0.33$), coefficient of friction ($\mu = 0.7$), pad radius (4.955 mm), and the length of the flat pad (6.466 mm). The normal forces P and tangential forces Q on the contact surfaces, as well as the bulk stresses S in the disk, were obtained from the finite element analyses of the blade–disk assembly.

The pressure and tangential loads for individual steps of a mission as given by FEM analyses were used to compute the contact stresses at the trailing edge of contact for various depths beneath the contact surface. The contact stresses were then summed with the bulk stress to obtain the total stress profile along a specified direction. For illustration, the computed total stress profiles for the high-pressure side (Hi01) at load step 1 and 2 of the mission are presented in Fig. 8.

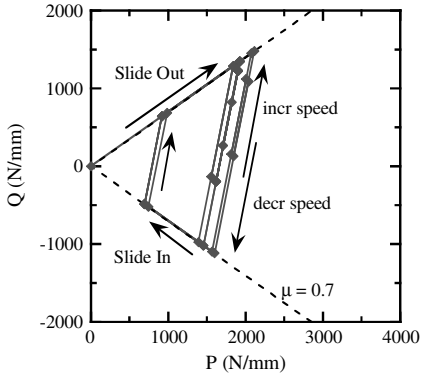

Fig. 7 Representative P and Q history for the typical fan speed profile shown in Fig. 6.

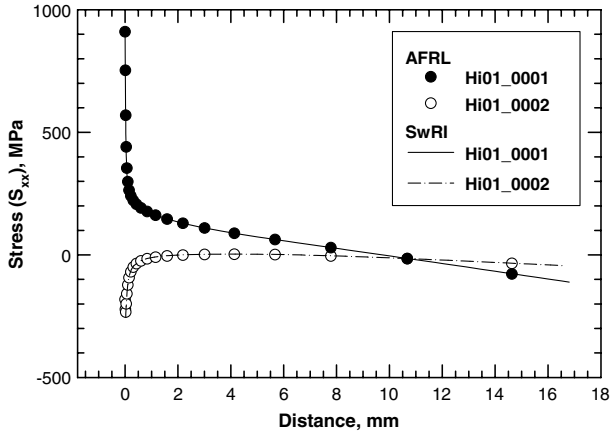

Fig. 8 Computed total stress values at high-pressure side for mission load steps 1 and 2.

Load step 1 resulted in a tensile stress at the trailing edge of contact because of a positive (clockwise) shear force, while step 2 resulted in a compressive stress due to a negative (counterclockwise) shear force. The stress profiles associated with the remaining load increments were different in magnitude but similar in shape to the profiles illustrated in Fig. 8 (they were not included due to paper length limitations). In the WCF computations, the moments acting on the blade were ignored, whereas the CAPRI computations included the moments. For both load steps, the total stresses computed by CAPRI and WCF were essentially identical except near the edge of contact on the surface ($y = 0$), as shown in Fig. 8. The WCF formulation predicted slightly higher stresses near the edge of contact surface at a distance less than 5 μm from the surface. This was probably due in part to ignoring the contact moment. At a crack depth of about 1.5 mm, the contact stress diminished to very low values and the total stress equaled the bulk stress.

B. Model Calibration

When failure data are available, the probability of fretting failure can be estimated from a direct fit of the data. However, to quantify the influence of inspection, a physics-based probabilistic model is required to estimate the random sizes of propagating cracks. The probabilistic model can be calibrated to match the component failure data, and can be used to quantify the influence of surface treatments on the probability of fracture.

Information regarding a number of random variables is typically required to perform a probabilistic fracture assessment. These variables can be categorized into six primary groups related to the size and location of the initial crack, variability associated with applied stress values and crack growth life models, and uncertainty in the frequency and quality of nondestructive inspection [3,35]. For this example, data were not available to characterize these variables. However, previous depot inspections revealed premature cracking in some disks, shown in Fig. 9a. For the calibration process it was assumed that the scatter in the measured crack areas was solely due to the variability in the fretting stress. A fretting stress scatter random variable was introduced to account for this uncertainty. Using the stress values from the FE results, crack area versus flight hour values were computed using the DARWIN probabilistic fracture mechanics software [35]. To quantify individual values of the fretting stress scatter random variable, deterministic fretting stress bias values were applied to the FE stress values and adjusted so that the crack areas computed using DARWIN were identical to the measured crack areas. The distribution of the resulting fretting stress scatter variable is shown in Fig. 9b, in which it was assumed that this variable was lognormally distributed.

To calibrate fracture risk, the anomaly occurrence rate was set equal to the ratio of the number of cracked disks to the total number of disks in the population. The probability of fracture was computed using DARWIN based on the stress values from the FE results, the

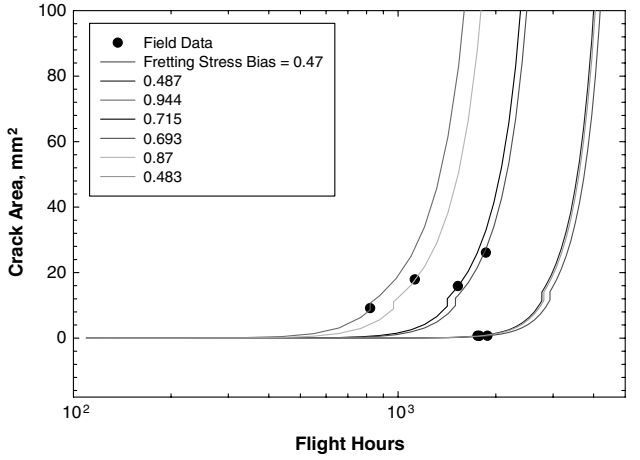

a)

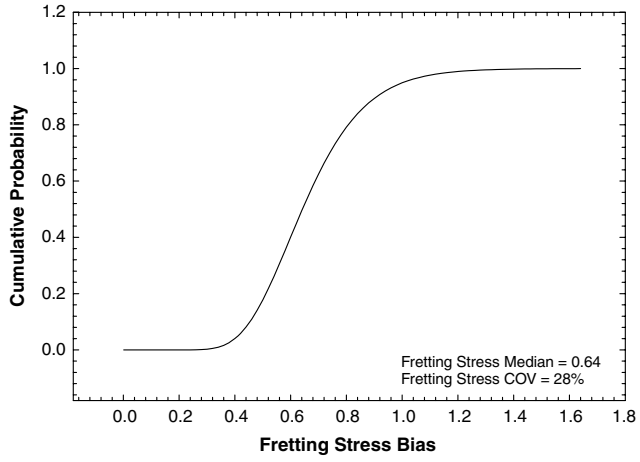

b)

Fig. 9 Calibration of the stress scatter random variable: a) deterministic fretting stress bias values were applied to the FE stress values and adjusted so that the simulated crack areas were identical to the measured crack areas and b) distribution of the resulting fretting stress scatter variable.

calibrated fretting stress scatter factor, and the calibrated anomaly occurrence rate. The crack growth lives of the measured cracks were estimated from the DARWIN results shown in Fig. 9a. The results are shown in Fig. 10. Also shown in Fig. 10 are Weibull and lognormal distributions based on the estimated crack growth lives associated with the measured cracks. There was reasonable agreement among the lives estimated from failure data with the probabilistic fracture risk estimates, as expected.

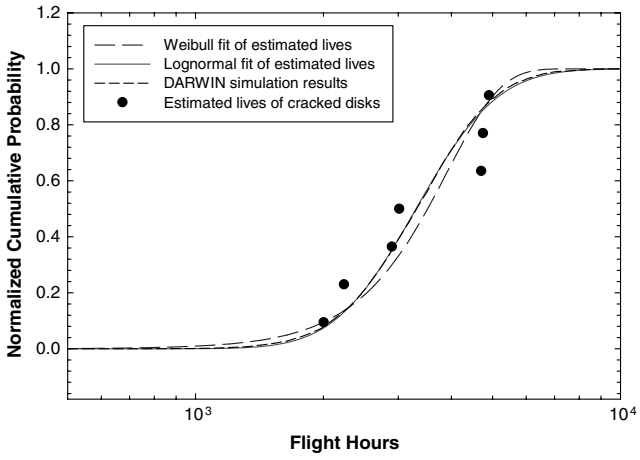

Fig. 10 Comparisons of lives estimated from failure data with probabilistic fracture risk estimates.

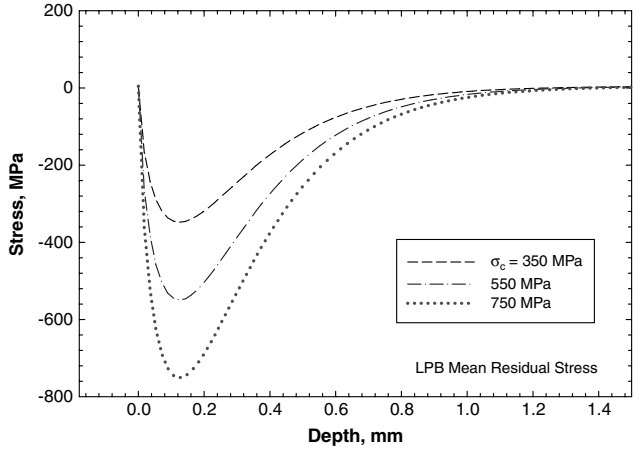

Fig. 11 Deterministic residual stress profiles associated with various degrees of relaxation.

C. Influences of Deterministic Residual Stress Values

The influence of residual stresses associated with LPB on the risk of fracture of an engine disk was investigated using the calibrated model described in the previous section. It is well known that residual stresses may relax over time due to temperature, overloads, or applied fretting stresses. The σ_c parameter of Eq. (4) was adjusted to low (350 MPa), medium (550 Mpa), and high (750 MPa) values to illustrate several residual stress profiles resulting from various degrees of relaxation, shown in Fig. 11. These values were combined with the FE fretting and bulk stresses (Fig. 12) and applied to fracture risk assessment. The results are shown in Fig. 13, in which it can be observed that the risk reduction is substantial for the medium and high σ_c values. Even the low value of σ_c provides a substantial risk reduction in the early stage of life, which suggests that the residual stress influence can be of some benefit after significant relaxation has occurred.

One of the objectives of this study was to quantify the influence of inspection on the probability of fracture. Two nondestructive inspection techniques were considered: eddy current, and fluorescent penetrant inspection (FPI). The probability of detection curves for the selected inspection methods are shown in Fig. 14. The influence of FPI inspection performed every 2000 flight hours is shown in Fig. 13, in which it can be observed that the risk reduction is substantial, particularly when surface treatment is performed. It is interesting to note that when the inspections are performed, the risk

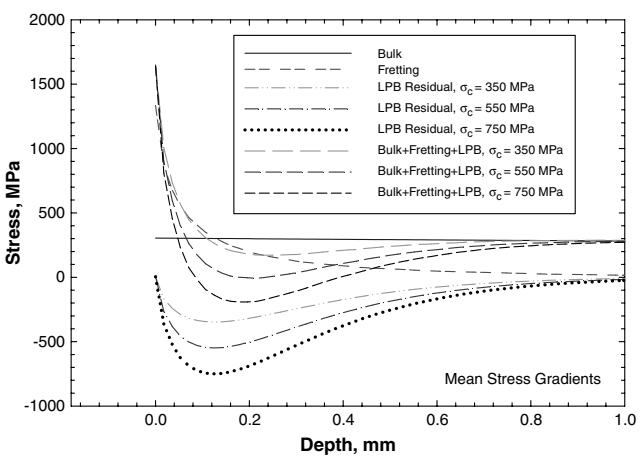

Fig. 12 Combined deterministic stress values for the maximum load step associated with the mission shown in Fig. 6.

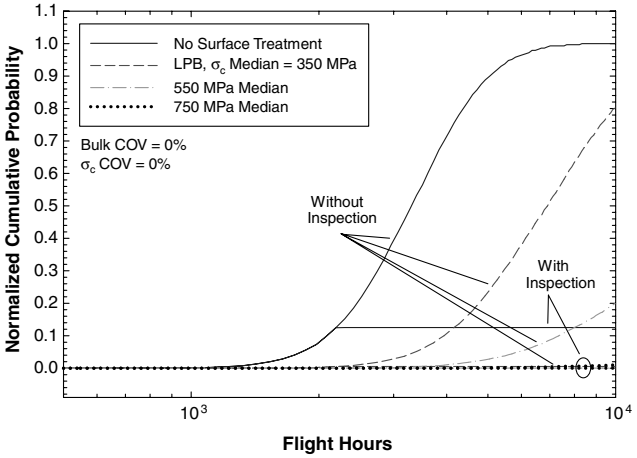

Fig. 13 Influence of deterministic residual stress values on normalized probability of fracture for several degrees of relaxation.

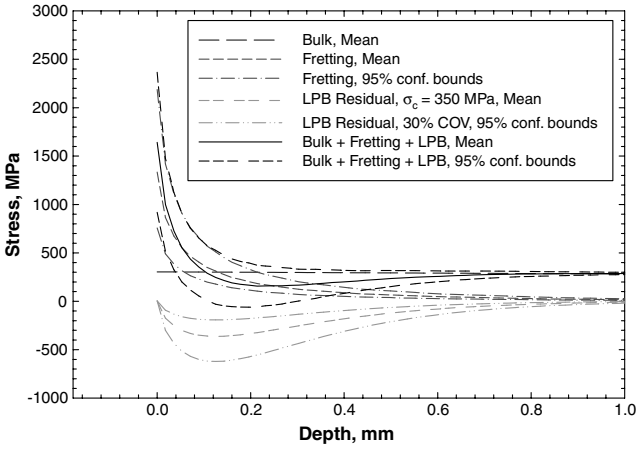

Fig. 16 Combined random stress values for the maximum load step associated with the mission shown in Fig. 6.

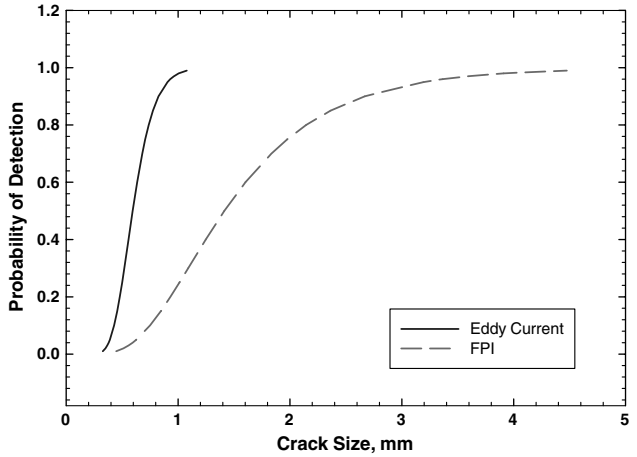

Fig. 14 Probability of detection distributions for representative eddy current and FPI methods.

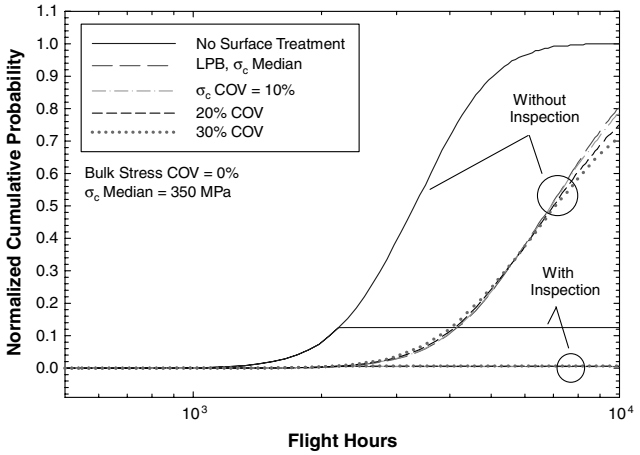

Fig. 17 Influence of random residual stress values on normalized probability of fracture for several values of residual stress COV.

reduction associated with the various residual stress curves are very similar, which again indicates that the surface treatment can be beneficial even when substantial relaxation has occurred.

D. Influences of Random Residual Stress Values

The influence of random residual stresses associated with LPB on the risk of fracture was also investigated. The σ_c parameter of Eq. (4) was modeled as a lognormal random variable with a median value of 350 MPa and coefficient of variation (COV) values of 10, 20, and 30%. Residual stress profiles (Fig. 15) were combined with the FE fretting and bulk stresses (Fig. 16) and applied to fracture risk assessment. The results (Fig. 17) show that risk reduction is nearly identical for the three substantially different COV values, both with and without inspection.

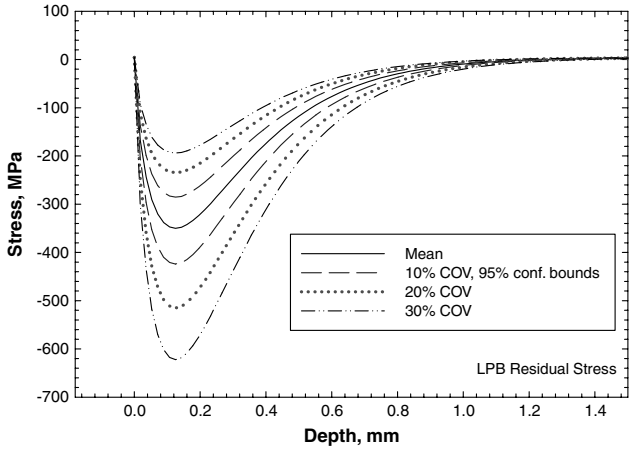

Fig. 15 Random residual stress profiles associated with several values of residual stress COV.

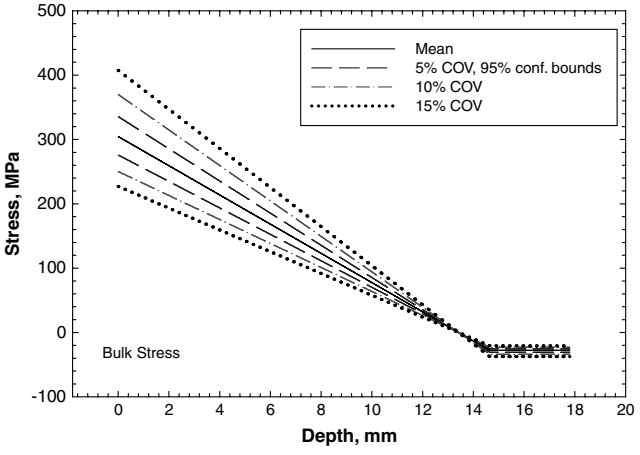

Fig. 18 Random bulk stress profiles associated with several values of bulk stress scatter factor COV.

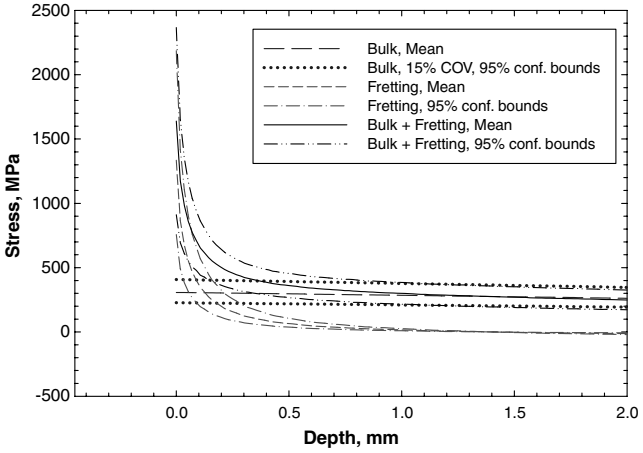

Fig. 19 Combined random stress values for the maximum load step associated with the mission shown in Fig. 6.

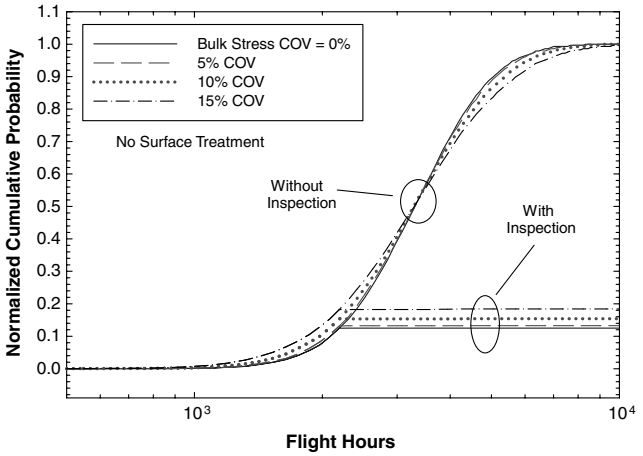

Fig. 20 Influence of random bulk stress values on normalized probability of fracture for several values of bulk stress scatter factor COV.

E. Influences of Random Bulk Stress Values

The probabilistic model was calibrated assuming that bulk stress was a deterministic quantity. However, since it is expected that the bulk stress may be random, the influence of random bulk stresses on the risk of fracture was also investigated. A bulk stress scatter random variable was introduced as a lognormal random variable with a median value of 1.0 and COV values of 5, 10, and 15%. Bulk stress profiles associated with this variable are shown in Fig. 18. These values were combined with the FE fretting and bulk stresses (Fig. 19) and applied to fracture risk assessment. The results (Fig. 20) show that risk is somewhat sensitive to the bulk stress COV value, and is dependent on the design life value.

VI. Conclusions

An approach was presented for estimating the risk reduction associated with surface treatments of aircraft engine components subjected to fretting fatigue. The approach centered on the estimation of contact stress values associated with fretting in the disk–blade interface of a typical gas turbine engine. Initial fracture risk results suggest that surface treatments have the potential to significantly reduce the probability of fracture associated with fretting fatigue for the range of values considered under this study, particularly when combined with nondestructive inspection. Further investigation is required to assess the influences of additional factors such as dynamic loading effects.

Acknowledgments

This work was supported by NAVAIR under agreement EDO-08-SA-0021. The authors wish to acknowledge Sam Naboulsi for performing the fine mesh finite element computations at the Air Force Research Laboratory Major Shared Resource Center at Wright–Patterson Air Force Base.

References

[1] Federal Aviation Administration, "Advisory Circular: Damage Tolerance for High-Energy Turbine Engine Rotors," U.S. Dept. of Transportation Rept. AC 33.14-1, Washington, DC, 2001.

[2] Federal Aviation Administration, "Advisory Circular: Damage Tolerance of Hole Features in High-Energy Turbine Engine Rotors," U.S. Dept. of Transportation Rept. AC 33.70-X, Washington, DC, 2008.

[3] Wu, Y. T., Enright, M. P., and Millwater, H. R., "Probabilistic Methods for Design Assessment of Reliability with Inspection," *AIAA Journal*, Vol. 40, No. 5, 2002, pp. 937–946. doi:10.2514/2.1730

[4] Szolwinski, M. P., and Farris, T. N., "Mechanics of Fretting Fatigue Crack Formation," *Wear*, Vol. 198, Nos. 1–2, 1996, pp. 93–107. doi:10.1016/0043-1648(96)06937-2

[5] Cowles, B. A., "High Cycle Fatigue in Aircraft Gas Turbines: An Industry Perspective," *International Journal of Fracture*, Vol. 80, Nos. 2–3, 1989, pp. 147–163. doi:10.1007/BF00012667

[6] Nicholas, T., and Zuiker, J. R., "On the Use of the Goodman Diagram for High Cycle Fatigue Design," *International Journal of Fracture*, Vol. 80, Nos. 2–3, 1989, pp. 219–235. doi:10.1007/BF00012670

[7] Enright, M. P., McClung, R. C., Hudak, S. J., and Francis, W. L., "Probabilistic Treatment of Crack Formation and Growth for Gas Turbine Engine Materials," 51st ASME International Gas Turbine and Aeroengine Technical Congress, American Society of Mechanical Engineers Paper GT2006-90813, Barcelona, 8–11 May 2006.

[8] Zhang, R., and Mahadevan, S., "Probabilistic Prediction of Fretting Fatigue Crack Nucleation Life of Riveted Lap Joints," 41st AIAA Structures, Dynamics, and Materials Conference, AIAA Paper 2000-1645, Atlanta, 3–6 April 2000.

[9] Frost, N. E., Marsh, K. J., and Pook, L. P., *Metal Fatigue*, Oxford Univ. Press, Oxford, 1974.

[10] Hills, D. A., and Nowell, D., *Mechanics of Fretting Fatigue*, Kluwer, Dordrecht, The Netherlands, 1994.

[11] Nicholas, T., "Critical Issues in High Cycle Fatigue," *International Journal of Fatigue*, Vol. 21, 1999, pp. S221–S231. doi:10.1016/S0142-1123(99)00074-2

[12] Waterhouse, R. B., "Avoidance of Fretting Fatigue," *Fretting Fatigue*, edited by R. B. Waterhouse, Applied Science, London, 1981, pp. 221–240.

[13] Rayaproula, D., and Cook, R., "A Critical Review of Fretting-Fatigue Investigations at the Royal Aerospace Establishment," *Standardization of Fretting-Fatigue Test Methods and Equipment*, edited by M. Delmi and R. Waterhouse, American Society for Testing and Materials, Philadelphia, 1992, pp. 129–152.

[14] Waterhouse, R., "Fretting Fatigue," *International Materials Reviews*, Vol. 37, No. 2, 1992, pp. 77–97.

[15] Lindley, T. C., "Fretting Fatigue in Engineering Alloys," *International Journal of Fatigue*, Vol. 19, No. 93, 1997, pp. 39–49. doi:10.1016/S0142-1123(97)00039-X

[16] Antoniou, R. A., and Radtke, T. C., "Mechanisms of Fretting-Fatigue of Titanium Alloys," *Materials Science and Engineering A*, Vol. 237, No. 2, 1997, pp. 229–240. doi:10.1016/S0921-5093(97)00419-X

[17] Chan, K. S., Lee, Y-D., Davidson, D. L., and Hudak, S. J., "A Fracture Mechanics Approach to High Cycle Fretting Fatigue Based on the Worst Case Fret Concept: 2. Experimental Evaluation," *International Journal of Fracture*, Vol. 112, No. 4, 2001, pp. 331–353. doi:10.1023/A:1013519825958

[18] Faanes, S., and Fernando, U., "Life Prediction in Fretting Fatigue Using Fracture Mechanics," *Fretting Fatigue*, Mechanical Engineering, London, 1994, pp. 149–159.

[19] Dini, D., Nowell, D., and Dyson, I. N., "The Use of Notch and Short Crack Approaches to Fretting Fatigue Threshold Prediction: Theory and Experimental Validation," *Tribology International*, Vol. 39, No. 10, 2006, pp. 1158–1165. doi:10.1016/j.triboint.2006.02.033

[20] Nowell, D., and Araujo, J. A., "Small Crack Methodologies and Crack Arrest in Fretting Fatigue," *Small Fatigue Cracks: Mechanics, Mechanisms, and Applications*, edited by K. S. Ravichandran, R. O. Ritchie, and Y. Murakami, Elsevier Science, Oxford, 1999, pp. 361–372.

[21] Prevey, P. S., "The Effect of Low Plasticity Burnishing (LPB) on the HCF Performance and FOD Resistance of Ti-6Al-4V," Sixth National Turbine Engine High Cycle Fatigue (HCF) Conference, Jacksonville, FL, 5–8 March 2001.

[22] Millwater, H., John, J., Larsen, J., and Buchanan, D., "Probabilistic Modeling of Residual Stress Data of IN100," 49th AIAA/ASME/ASCE/AHS/ASC Structures, Structural Dynamics, and Materials Conference, AIAA Paper 2008-1983, Schaumburg, IL, 2008.

[23] Prevey, P. S., Jayaraman, N., and Shepard, M. J., "Improved HCF Performance and FOD Tolerance of Surface Treated Ti-6-2-4-6 Compressor Blades," Ninth National Turbine Engine High Cycle Fatigue Conference, Pinehurst, NC, 2004.

[24] Martinez, S. A., Sathish, S., Blodgett, M. P., Mall, S., and Namjoshi, S., "Effects of Fretting Fatigue on the Residual Stress of Shot Peened Ti-6Al-4V Samples," *Materials Science and Engineering A*, Vol. 399, Nos. 1–2, 2005, pp. 58–63. doi:10.1016/j.msea.2005.02.028

[25] McClung, R. C., "A Literature Survey on the Stability and Significance of Residual Stresses During Fatigue," *Fatigue and Fracture of Engineering Materials and Structures*, Vol. 30, No. 3, 2007, pp. 173–205. doi:10.1111/j.1460-2695.2007.01102.x

[26] Konig, G. W., "Life Enhancement of Aero Engine Components by Shot Peening: Opportunities and Risks," *Shot Peening*, edited by L. Wagner, Wiley, Weinheim, Germany, 2003, pp. 13–23.

[27] Rodopoulos, C. A., Edwards, R. E., Curtis, S., Romoero, J. S., Choi, J-H., de los Rios, E., and Levers, A., "Theoretical Analysis of Beneficial and Detrimental Effects of Controlled Shot Peening in High Strength Aluminum Alloys," *Shot Peening*, edited by L. Wagner, Wiley, Weinheim, Germany, 2003, pp. 547–553.

[28] Calcaterra, J., and Naboulsi, S., "Design Methodology to Investigate Contact Fatigue Damage in Turbine Engine Hardware," *International Journal of Fatigue*, Vol. 27, No. 9, 2005, pp. 1133–41.

[29] Golden, P. J., and Calcaterra, J., "A Fracture Mechanics Life Prediction Methodology Applied to Dovetail Fretting," *Tribology International*, Vol. 39, No. 10, 2006, pp. 1172–80.

[30] Gean, M. C., and Farris, T. N., "Finite Element Analysis of the Mechanics of Blade/Disk Contacts," 46th AIAA Structures, Structural Dynamics, and Materials Conference, AIAA Paper 2005-1907, Austin, TX, 18–21 April 2005.

[31] McVeigh, P. A., Harish, G., Farris, T. N., and Szolwinski, M. P., "Modeling Interfacial Conditions in Nominally Flat Contacts for Application to Fretting Fatigue of Turbine Engine Components," *International Journal of Fatigue*, Vol. 21, 1999, pp. 157–165. doi:10.1016/S0142-1123(99)00067-5

[32] Chan, K. S., Lee, Y-D., Davidson, D. L., and Hudak, S. J., "A Fracture Mechanics Approach to High Cycle Fretting Fatigue Based on the Worst Case Fret Concept: 1. Model Development," *International Journal of Fracture*, Vol. 112, No. 4, 2001, pp. 299–330. doi:10.1023/A:1013507425050

[33] Ciavarella, M., Hills, D. A., and Monno, G., "The Influence of Rounded Edges on Indentation by a Flat Punch," *Proceedings of the Institution of Mechanical Engineers, Journal of Mechanical Engineering Science, Part C*, Vol. 212, No. 4, Part C, 1998, pp. 319–328.

[34] Tufft, M. K., "Modeling of Fatigue Behavior due to Shot Peening Conditions," *Shot Peening*, edited by L. Wagner, Wiley, Weinheim, Germany, 2003, pp. 530–539.

[35] "DARWIN User's Guide," Southwest Research Institute, San Antonio, TX, 2008.

[36] Golden, P. J., "Development of a Dovetail Fretting Fatigue Fixture for Turbine Engine Materials," *International Journal of Fatigue* (to be published).

[37] "ABAQUS Documentation," Simulia, Providence, RI, 2007.

A. Pelegri
Associate Editor